RSC Advances

PAPER

View Article Online
View Journal | View Issue

Cite this: *RSC Adv.*, 2025, **15**, 45874

Green synthesis of ZnO nanoparticles using *Justicia adhatoda* for effective photocatalytic degradation of methylene blue dye

Ashraful Bari Anik, [a] Mofassel Hossen Akash,[a] Md. Ashraful Alam,[a] Md. Zahangir Alam, [b] Debanjon Sarker[c] and Nahid Sultana *[a]

The proposed eco-friendly technique for synthesizing zinc oxide nanoparticles (ZnO NPs) shows significant potential due to its sustainability, no detrimental impacts, ecological safety, and non-toxicity. In this study, ZnO NPs were synthesized using *Justicia adhatoda* leaf extract as a reducing and stabilizing agent, leveraging its phytochemical richness to obtain highly crystalline nanoparticles with diverse morphologies, which are used as a photocatalyst to degrade methylene blue (MB) dye. The characterization of prepared ZnO NPs was conducted using XRD, UV-Vis, FTIR, FESEM, and EDX analysis. Optical characterization indicated strong absorption in the UV region (371 nm) with a suitable band gap (3.04 eV) for photocatalysis. The hexagonal wurtzite crystallite size (18.57 nm) was confirmed through XRD pattern analysis. FESEM investigation revealed a rough flower-like morphology with an average particle size of 75 nm. The FTIR spectrum confirmed the presence of Zn–O stretching vibrations, as confirmed by the characteristic peak observed at 693 cm^{-1}. The biosynthesized ZnO NPs exhibited excellent photocatalytic performance in degrading methylene blue under natural sunlight, achieving nearly complete removal under optimized conditions. The degradation process followed pseudo-first-order kinetics, possessing a rate constant of 0.037 min^{-1}. Overall, this work highlights a sustainable and low-cost method for fabricating ZnO-based photocatalysts, offering significant promise for environmental remediation.

Received 4th September 2025
Accepted 17th November 2025

DOI: 10.1039/d5ra06656e

rsc.li/rsc-advances

1. Introduction

The release of untreated or inadequately treated textile wastewater into water bodies poses a serious threat to aquatic life, human health, and the overall health of the environment.[1] Methylene blue (MB) dyes find extensive applications across various industries, such as textiles, pharmaceuticals, food, tanneries, leather, and cosmetics. They play a crucial role in industrial wastewater contributions. Traditional systems for treating industrial wastewater exhibit certain limitations, particularly in their ability to effectively manage dye wastewater.[2,3] The yearly output of textile dyes is expected to exceed 700 000 tons, with azo dyes constituting 60–70% of this total.[4] The dyes exhibit a high level of resistance to natural degradation, persisting in the environment for extended periods due to their composition, and around 15–50% release of these dyes into the wastewater significantly increases the chemical oxygen demand (COD) and biological oxygen demand (BOD), which are considerably higher than the safe discharge standards.[5] The physicochemical properties of water are disturbed by azo dyes, which change the pH (usually between 10 and 11 for dye effluents) and introduce a large concentration of inorganic chemicals, having a major impact on aquatic ecosystems.[6] Their intricate chemical architectures, which include aromatic rings and azo linkages (–N=N–), make them even more resistant to breakdown by standard approaches of water purification.[7] Because of this resistance, we need effective and novel ways to remove them, especially ones that can deal with their toxicity and bioaccumulation potential.[8]

New materials and methods for water purification have emerged as a result of significant progress in nanoscience and nanotechnology. One area of focus is the elimination of harmful dyes from industrial effluents. Promising options for wastewater treatment include materials with exceptional photocatalytic capabilities, such as graphitic carbon nitride (g-C_3N_4), bismuth vanadate ($BiVO_4$), zinc oxide (ZnO), and titanium dioxide (TiO_2).[9] Because of their capacity to mineralize organic contaminants into ecologically safe byproducts like water and carbon dioxide, advanced oxidation processes (AOPs) such as

[a]*Department of Applied Chemistry & Chemical Engineering, Noakhali Science and Technology University, Noakhali-3814, Bangladesh. E-mail: ashraful.anik3100@gmail.com; akash0414@student.nstu.edu.bd; ashraf.acce@nstu.edu.bd; nahidsultana@nstu.edu.bd; Tel: +880-1935470356*

[b]*Department of Applied Chemistry & Chemical Engineering, University of Dhaka, Bangladesh. E-mail: zahangir@du.ac.bd*

[c]*Department of Chemical Engineering, Bangladesh University of Engineering and Technology, Bangladesh. E-mail: debanjon14sarker@gmail.com*

ozonation, sonochemical degradation, electrochemical remediation, heterogeneous photocatalysis, and Fenton oxidation have arisen as revolutionary methods.[10] In order to break down complex dye molecules, these activities produce reactive oxygen species (ROS), such as hydroxyl radicals ($OH^{\bullet}$) and superoxide anions ($O_2^{-\bullet}$).[7]

ZnO stands out from other top-performing photocatalytic materials, including TiO_2, g-C_3N_4, $BiVO_4$, ZnS, and CeO_2, due to its unique properties.[11] Ensuring efficient charge carrier generation and prolonged exciton stability, ZnO outperforms TiO_2, $BiVO_4$, g-C_3N_4, ZnS, and CeO_2 in minimizing electron–hole recombination. Its wide direct bandgap of approximately 3.37 eV and high excitation binding energy of 60 meV contribute to charge carrier generation and prolong excitation stability of ZnO.[12,13] For photocatalytic activity to be maintained when exposed to UV light, this characteristic is essential. ZnO has more exceptional electrical and optical properties than those of TiO_2, CeO_2, g-C_3N_4, and $BiVO_4$, along with extraordinary chemical and thermal flexibility. This longevity is in contrast to materials like ZnS and $BiVO_4$ that are photo-corrosion prone or have weak water stability.[14] In photodegradation applications, ZnO is a better alternative than CeO_2 because of its oxygen storage capacity and redox characteristics; however, the relatively narrow bandgap can cause unwanted secondary reactions.[15]

Photocatalytic wastewater treatment is only one example of how green synthesis has become more popular as a way to create high-tech nanomaterials without negatively impacting the environment.[16] This approach is a greener alternative to traditional methods like sol–gel, co-precipitation, and chemical vapor deposition since it uses bioactive phytochemicals found in plant extracts instead of harmful chemicals and energy-intensive procedures.[17–19] The synthesis of nanoparticles using various plants, including *Azadirachta indica*,[20] *Catharanthus roseus*,[21] *Aloe vera*,[22] *Myristica fragrans*,[23] *Ficus carica*,[24] *Punica granatum*,[25] and *Sesbania grandiflora*.[26] All the plant-based resources studied, *J. adhatoda*'s therapeutic qualities and abundant phytochemical composition make it an attractive prospect for NPs production.[27] *J. adhatoda* extract has a lot of stuff that helps in synthesizing ZnO NPs, like alkaloids, flavonoids, and tannins, with vasicine.[28,29] The phytochemicals' capping effect guarantees particle stabilization and inhibits aggregation, and these bioactive components make it easier to reduce zinc ions (Zn^{2+}) into zinc oxide (ZnO). The phytochemical diversity of the plant is important for sustainable nanotechnology since it helps with synthesis and gives chances to adjust the properties of NPs to suit specific application needs.[30,31]

This study presents the biogenic synthesis of ZnO NPs using *J. adhatoda*, with a focus on their application in the photocatalytic degradation of methylene blue (MB) dye. The use of green synthesis not only enhances the functional properties and environmental compatibility of the ZnO NPs but also results in improved photocatalytic performance. The synthesized nanoparticles were extensively characterized and demonstrated high catalytic efficiency, making them promising candidates for wastewater treatment. The method is simple, cost-effective, non-toxic, and eco-friendly, yielding a potent photocatalyst with minimal environmental impact.

2. Materials and methods

2.1 Materials

Justicia adhatoda leaves collected from the premises of Noakhali Science & Technology University. Analytical grade Zinc nitrate hexahydrate ($Zn(NO_3)_2 \cdot 6H_2O$) was used as precursor of zinc nanoparticles. Ethanol of 99.9% purity supplied by Merck, Germany was used for the extraction of phytochemicals from collected leaves as well as for washing of synthesized ZnO NPs. Distilled water collected from lab, sodium hydroxide pellets (NaOH), Assay 98.0%, supplied by Lobachemie, India was used for pH adjustment during synthesis of nanoparticles. Methylene Blue dye used as model pollutant. All chemicals are collected from local market in Dhaka, Bangladesh.

2.2 Methods

2.2.1 Collection and preparation of plant extract. The *J. adhatoda* leaves were collected from the garden of Noakhali Science and Technology University in Bangladesh. The recently collected leaves were meticulously rinsed multiple times with tap water, subsequently followed by deionized water. The leaves were air-dried in the shade for 3 days, exposed to oven drying for 3 h, and subsequently milled into a fine powder. 10 g of specimen of the powder was subjected to boiling in 100 mL of deionized water at 60 °C for 45 min. The resultant extract was filtered with Whatman No. 1 filter paper. The filtrate was centrifuged to guarantee the total elimination of residual leaf particles and subsequently stored at 4 °C in a refrigerator for future use.

2.2.2 Green synthesis of ZnO NPs. Green ZnO NPs have been synthesized by using zinc nitrate hexahydrate ($Zn(NO_3)_2 \cdot 6H_2O$) as the precursor. 20 mL of *J. adhatoda* leaves extract was added dropwise with 100 mL of 0.1 M $Zn(NO_3)_2 \cdot 6H_2O$ solution under constant stirring at 250 rpm at room temperature. During stirring, 1 M of sodium hydroxide (NaOH) solution was dropping into the solution mixture until the pH of the solution was turned into 11. The solution underwent continuous stirring for 2 h at room temperature. The formation of ZnO NPs was indicated by the appearance of a light yellowish precipitate during continuous stirring of the reaction mixture. Centrifugation of the reaction mixture at 8000 rpm for a duration of 20 min facilitated the collection of the final product. The precipitate was then subjected to multiple washing steps (3–4 times) with distilled water and then with ethanol to remove any extraneous impurities or unreacted components from the surface of the biosynthesized nanomaterial. The precipitate was dried at 60 °C for 24 h before calcination. To enhance crystallinity, the dried ZnO NPs were subjected to annealing in a muffle furnace at a temperature of 500 °C for a duration of 3 h. This process yielded a fine white colored powder of ZnO NPs, which was subsequently utilized for further investigations and surface characterization followed by applications. The aqueous extract of *J. adhatoda* contains a variety of phytochemicals, including

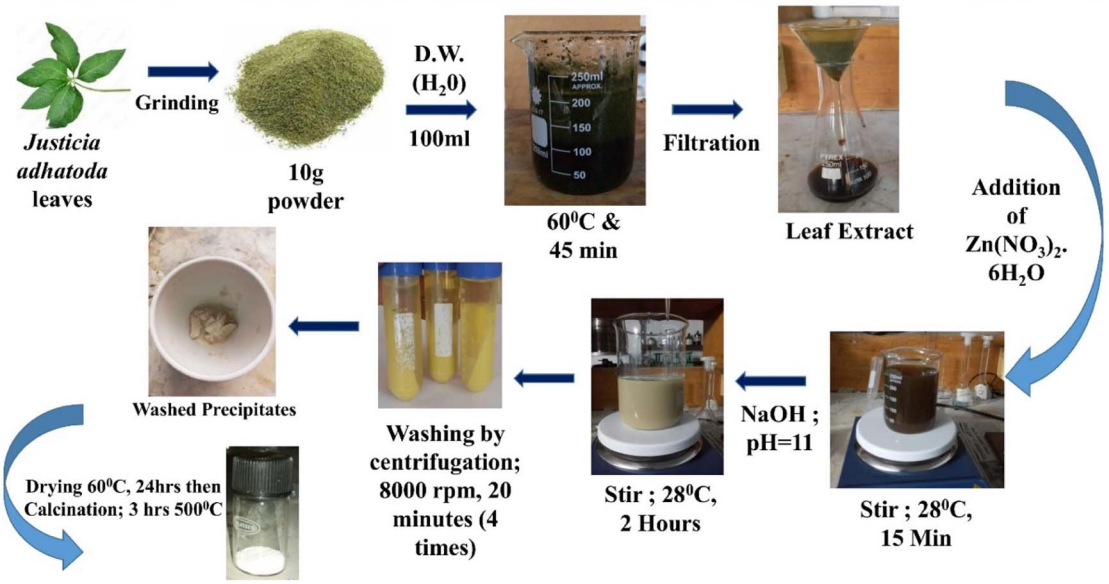

Fig. 1 Green synthesis of ZnO NPs from *Justicia adhatoda* leaf extract.

flavonoids and tannins, which play crucial roles in nanoparticle synthesis. These compounds, rich in –OH groups, act as reducing agents, converting zinc nitrate into $Zn(OH)_2$. Subsequently, high-temperature annealing transforms $Zn(OH)_2$ into ZnO NPs. This two-step process, involving chelation between zinc ions and phytochemicals followed by thermal conversion, ultimately leads to the formation of green synthesized ZnO NPs depicted in Fig. 1.[32]

2.2.3 Photocatalytic degradation test. The photocatalytic degradation of MB aqueous solution in direct sunlight on clear sunny days between 11 am and 2 pm during the October–November 2024 period, when the average daily temperature was 31 ± 2 °C and the UV index was 6–8. Solar light irradiation was used to assess the photocatalytic activity of the prepared photocatalysts. An adsorption–desorption equilibrium was established by sonication of varying amounts of each synthesized nanoparticle in 100 mL of MB aqueous solution, followed by keeping the mixture in darkness for 30 min. Before exposure to sunlight, the photocatalytic performance of each nanoparticle was assessed in a dark environment, and the UV-visible spectrum of the samples was recorded at the initial time point. The nanoparticle-containing solutions were exposed to natural sunlight for 120 min at 20 min intervals. After each exposure, the solutions were centrifuged to precipitate the nanoparticles, which could otherwise interfere with UV-Vis absorbance measurements. The degradation efficiency of MB was assessed by capturing the absorption spectra of the test dye and quantifying the absorption intensity at the typical peak of 664 nm with a UV-Vis spectrophotometer. The catalytic removal efficiency of MB dye by the manufactured photocatalysts was ultimately estimated using the eqn (1) presented below.

$$\text{Degradation efficiency } (\%) = \frac{A_0 - A_t}{A_0} \times 100\% \quad (1)$$

A_0 and A_t denote the absorbance of the dye solution prior to and after the photocatalytic reaction, respectively. The kinetics of the photocatalytic degradation process were assessed utilizing the Langmuir–Hinshelwood equation, and the resultant linear representation signifies the reaction order (k). A_t denotes the concentration of MB with photocatalysts at different time intervals, whereas A_0 signifies the initial concentration of MB without photocatalysts. A stock solution of MB (1000 ppm) was produced for the kinetic analysis and subsequently diluted to concentrations of 10, 15, 20, 30, and 40 ppm.

2.2.4 Characterization. The characterization of the synthesized nanoparticles is a key focus of this study, aimed at gaining a deeper understanding of their properties. Absorbance measurement was carried out on a PerkinElmer Lambda 365+ UV-Vis Spectrometer at a wavelength of 180–1100 nm. FT-IR spectra of samples were recorded on an FT-IR 8400S spectrophotometer (Shimadzu Corporation, Japan) in the wave number range of 4000–400 cm^{-1}, with a resolution of 4 cm^{-1} and scans of: 30. 100 mg of KBr and about 0.1 mg of samples were ground in a mortar, and the mixture was then compressed to create a pellet. The X-ray diffraction (XRD) patterns of the samples were obtained using an X-ray diffractometer (U1tima IV, Rigaku Corporation, Japan) at ambient temperature. Cu Kα radiation (λ = 0.154) from a broad-focus copper tube operating at 40 kV and 40 mA was utilized for the measurements. The XRD data were collected in continuous scanning mode with a scan speed of 3° per minute, covering a range from 10° to 80°. Bragg's law was employed to calculate the interplanar spacing of the crystalline samples. The structure of the samples was examined using an analytical field emission scanning electron microscope (JEOL JSM-7600F, Japan) at an accelerating voltage of 5.0 kV in back-scattered electron mode. To gain a deeper understanding of the structure, the microstructures of the samples were analyzed at four different magnifications. The EDS spectrum was utilized to

assess the elemental composition of the nanocomposite. Additionally, energy dispersive X-ray spectroscopy was performed using a field emission scanning electron microscope (JEOL JSM-7600F, Japan).

3. Results and discussion

3.1 X-ray diffraction analysis

The X-ray diffraction (XRD) analysis provides insights into the crystallite structure of biogenically synthesized ZnO NPs using *J. adhatoda* leaf extracts. The diffraction pattern, shown in Fig. 2(a), exhibits characteristic peaks at 2θ values of 31.88°, 34.56°, 36.37°, 47.67°, 56.72°, 63.01°, 66.56°, 68.09°, 69.20°, 72.77° and 77.09°, corresponding to the (100), (002), (101), (102), (110), (103), (200), (112), (201), (004) and (202) crystal planes respectively. These results confirm the formation of hexagonal wurtzite ZnO and are in good agreement with the standard reference data from JCPDS card no. 36-1451.[33] Which reports diffraction peaks at 31.7°, 34.4°, 36.2°, 47.5°, 56.6°, 62.8°, 67.9°, 72.6° and 68° for the corresponding planes.

Based on the X-ray diffraction (XRD) data of *J. adhatoda*/ZnO NPs, the crystallographic parameters and structural characteristics of the synthesized ZnO nanoparticles were carefully analyzed. The peaks observed in the XRD pattern were indexed according to their respective planes, and the crystallite sizes were determined using the Scherrer equation. The peak corresponding to the (100) plane at 31.88° exhibited a *d*-spacing of 2.8049 Å and a crystallite size of 18.57 nm showed in Table 1. This peak indicates the strong basal crystallinity of the ZnO nanoparticles, suggesting a well-organized and highly ordered structure. This reflection is a typical feature of the hexagonal wurtzite structure of ZnO, confirming the crystalline nature of the synthesized nanoparticles. At 34.56°, the (002) plane reflected a *d*-spacing of 2.5932 Å and a crystallite size of 21.02 nm. The (002) reflection aligns with the *c*-axis orientation of the ZnO nanoparticles, and the relatively larger crystallite size indicates preferential growth along this axis. This alignment along the *c*-axis is significant for potential applications in energy generation and light-emitting devices, as these properties are highly dependent on the crystallographic orientation. The (101) plane at 36.37° showed a *d*-spacing of 2.4682 Å and a crystallite size of 18.20 nm. This peak is important as it represents the overall crystallinity of the ZnO structure, providing insight into the nanoparticle quality. The crystallite size here further supports the idea of well-formed nanoparticles, with the size being similar to the other peaks, indicating uniformity in the crystallization process. The (102) plane at 47.67° exhibited a *d*-spacing of 1.9062 Å and a crystallite size of 17.05 nm. This

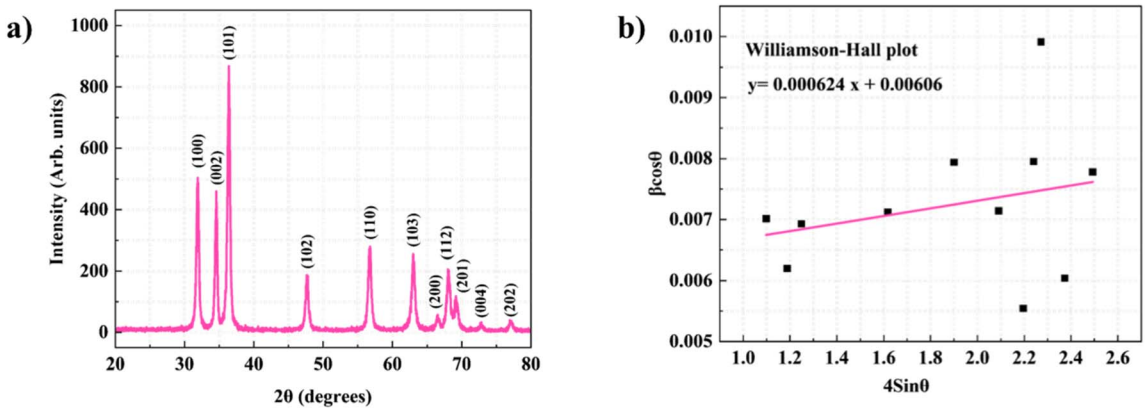

Fig. 2 (a) The XRD pattern of *J. adhatoda*/ZnO nanoparticles, and (b) Williamson–Hall plot of *J. adhatoda*/ZnO nanoparticles.

Table 1 Crystallographic parameters of *J. adhatoda*/ZnO NPs

S. no	2θ (degree)	FWHM (β) (degree)	Lattice planes (*hkl*)	Inter-planner spacing (*d*) (Å)	Crystallite size (*D*) (nm)
1	31.88	0.46221	(100)	2.8049	18.67
2	34.56	0.41346	(002)	2.5932	21.02
3	36.37	0.47978	(101)	2.4682	18.20
4	47.67	0.53205	(102)	1.9062	17.05
5	56.72	0.57573	(101)	1.6217	16.38
6	63.01	0.61367	(103)	1.4741	15.86
7	66.56	0.64608	(200)	1.4038	15.36
8	68.09	0.63763	(112)	1.3759	15.70
9	69.20	0.69171	(201)	1.3565	14.57
10	72.77	0.34321	(004)	1.2985	30.03
11	77.09	0.4946	(202)	1.2362	21.45
				***D* (average) = 18.57 nm**	

higher-order reflection suggests that the ZnO nanoparticles possess a well-defined structural symmetry and good packing along the planes.

The moderate crystallite size here further supports the notion of lateral atomic packing and structural stability. Similarly, the (101) reflection at 56.72° showed a *d*-spacing of 1.6217 Å and a crystallite size of 16.38 nm. This peak is another indicator of the lateral atomic packing within the ZnO structure. The smaller crystallite size here reflects possible distortions or strain effects within the nanoparticles, which is common in green-synthesized nanoparticles due to the influence of the plant extract. The (103) plane at 63.01° showed a *d*-spacing of 1.4741 Å and a crystallite size of 15.86 nm. This higher-order peak further supports the findings of well-ordered ZnO crystals, and the slightly reduced crystallite size indicates some variation in crystallinity along the (103) reflection. The (200) plane at 66.56° had a *d*-spacing of 1.4038 Å and a crystallite size of 15.36 nm. This peak indicates the extent of crystallinity, which contributes to the overall structural integrity of the nanoparticle. The (112) plane at 68.09° displayed a *d*-spacing of 1.3759 Å and a crystallite size of 15.70 nm. This peak is associated with minor lattice distortions and strain effects, providing insight into the elastic properties of the ZnO nanoparticles. The (201) plane at 69.20° exhibited a *d*-spacing of 1.3565 Å and a crystallite size of 14.57 nm. This peak represents a higher-order reflection and provides further evidence of the nanoparticle's crystalline nature. The (004) plane at 72.77° showed a *d*-spacing of 1.2985 Å and a crystallite size of 30.03 nm. This peak, indicative of long-range periodicity in the structure, demonstrates good crystallinity and structural order, which is typical of ZnO nanoparticles with higher symmetry. Finally, the (202) plane at 77.09° had a *d*-spacing of 1.2362 Å, and the crystallite size was 21.45 nm. This peak contributes to confirming the well-ordered nature of the ZnO nanoparticles and the overall crystalline phase.

The distinct and intense peaks clearly show that the ZnO nanoparticles synthesized by the reduction method using *J. adhatoda* leaf are crystalline. The outcomes are nearly identical to those that other researchers have found with zinc oxide nanoparticles. The typical crystallite was analyzed using the Debye–Scherrer equation:

$$D = k\lambda/\beta\cos\theta \quad (2)$$

where, D = crystalline size of nanoparticle, λ = wavelength of X-ray, β = full width of the peak at half maximum. K = Scherrer constant = 0.9 and θ = Bragg angle.

The average crystallite size (D) determined from the XRD peaks was 18.57 nm, indicating the formation of nanoparticles with uniform size and quantum confinement effects. This is consistent with the expected size range for ZnO nanoparticles synthesized through green synthesis methods, particularly with the use of *J. adhatoda* leaf extract as the reducing agent. These results highlight the well-defined crystalline structure of the nanoparticles, which can be further explored for various applications such as photocatalysis, sensing, and optical devices.

The Williamson–Hall (W–H) plot is used to analyze the broadening of X-ray diffraction (XRD) peaks to determine both the crystallite size and lattice strain in a material. The general equation for the Williamson–Hall method is

$$\beta_{hkl}\cos\theta = \frac{K\lambda}{D} + 4\sin\theta \quad (3)$$

where, β_{hkl} is the full-width at half maximum (FWHM) of the peak (in radians), corrected for instrumental broadening, θ is the Bragg angle, K is the shape factor (typically ~0.9), λ is the X-ray wavelength, D is the crystallite size, ε is the microstrain in the crystal.

In Fig. 2(b), the Williamson–Hall (W–H) plot equation obtained from this study is $y = 0.000624x + 0.00606$, which can be compared with the theoretical W–H equation: $\beta\cos\theta = (K\lambda/D) + 4\varepsilon\sin\theta$. Here, the slope of the linear fit (0.000624) corresponds to 4ε, allowing the calculation of the microstrain ($\varepsilon = 0.000156$). The intercept (0.00606) represents $K\lambda/D$, which is used to determine the crystallite size (D). A higher slope suggests a greater presence of lattice strain within the material, while a larger intercept indicates smaller crystallite sizes. This analysis provides a more comprehensive understanding of the material's structural properties compared to the Scherrer equation, as the W–H method accounts for both crystallite size and lattice strain.

The comparative analysis of XRD data for *J. adhatoda*/ZnO NPs highlights significant variations in crystallite size depending on the plant extract used presented in Table 2. In the current study, *J. adhatoda* leaf extract-mediated ZnO NPs exhibited a crystallite size of 18.57 nm. This indicates that synthesis conditions such as temperature, pH, and extract concentration play a crucial role in determining the final particle size.

Among the plant-mediated synthesis methods, *Azadirachta indica* (16 nm),[20] *Catharanthus roseus* (14 nm),[21] and *Ficus carica* (13 nm)[31] produced ZnO NPs with relatively smaller crystallite sizes. The use of *Aloe vera* (15.6 nm)[22] resulted in slightly larger particles, whereas *Myristica fragrans* (41.23 nm)[23] produced the largest crystallite size among the studied samples. The significantly larger size in *Myristica fragrans* suggests a weaker capping effect of its phytochemicals, allowing greater particle growth. Interestingly, *Punica granatum*-mediated synthesis yielded ZnO NPs with a size of 22 nm,[25] demonstrating a moderate crystallite size. The variation observed across different extracts could be attributed to the differences in phytochemical composition, which influences nucleation and growth mechanisms.

The hexagonal wurtzite crystal structure was consistently observed across all samples, confirming that the green synthesis approach preserves the fundamental crystal integrity of ZnO. However, the functional applications varied significantly, with *J. adhatoda*/ZnO NPs being particularly effective in photocatalytic degradation and reduction of organic compounds.[7] This suggests a strong surface reactivity, possibly due to a higher surface-area-to-volume ratio in smaller crystallites. Smaller crystallite sizes, such as the 5.2 nm ZnO NPs reported with *J. adhatoda* synthesis,[7] are advantageous in photocatalysis due to their enhanced charge separation efficiency. In contrast, larger nanoparticles, such as those

Table 2 Comparative XRD analysis of *J. adhatoda*/ZnO NPs with different plant extracts/ZnO NPs: synthesis method, crystallite size, crystal structure, and applications

S. no	Synthesis method	Extract used	Crystallite size (nm)	Crystal structure	Applications	References
1	Plant-mediated	*Azadirachta indica*	>33.97	Hexagonal wurtzite	Antimicrobial, photocatalytic	20
2	Plant-mediated	*Catharanthus roseus*	16	Hexagonal wurtzite	Anticancer, wound healing	21
3	Leaf extract-mediated	*Aloe vera*	25	Hexagonal wurtzite	Antibacterial	22
4	Leaf-extract mediated	*Myristica fragrans*	41.23	Hexagonal wurtzite	Antimicrobial, antioxidant	23
5	Leaf-extract mediated	*Ficus carica*	30	Hexagonal wurtzite	Bactericidal and photocatalytic	24
6	Fruit peel extract-mediated	*Punica granatum*	20	Hexagonal wurtzite	Antioxidant, antimicrobial	25
7	Leaf-extract mediated	*Sesbania grandiflora*	32–45	Hexagonal wurtzite	Antibacterial activity	26
8	Leaf-extract mediated	*J. adhatoda*	5.2	Hexagonal wurtzite	Photocatalytic degradation, reduction of organic compound	7
9	Leaf-extract mediated	*J. adhatoda*	18.57	Hexagonal wurtzite	Photocatalytic degradation	Current study

Table 3 Crystallographic parameters of *J. adhatoda*/ZnO NPs

Lattice constants	Standard values (Å)	Calculated values (Å)	*c*/*a* ratio	Standard volume (Å)^3	Calculated volume (Å)^3
$a = b$	3.249	3.239	1.0	47.62	47.12
c	5.206	5.186			

synthesized using *Myristica fragrans*,[23] might be more suited for antimicrobial applications due to their increased stability. Overall, the findings indicate that selecting an appropriate plant extract for ZnO NP synthesis can tailor the material's properties for specific applications. The variation in crystallite size, influenced by phytochemicals and synthesis conditions, underscores the versatility of green-synthesized ZnO NPs for biomedical and environmental applications.

The Table 3 shows calculated lattice constants for the biogenically synthesized ZnO nanoparticles were found to be $a = 3.239$ Å and $c = 5.186$ Å, with a corresponding unit cell volume of 47.12 Å^3. These values are slightly lower than the standard hexagonal wurtzite ZnO parameters ($a = 3.249$ Å, $c = 5.206$ Å, $V = 47.63$ Å^3, JCPDS No. 36-1451). The slight contraction in both a and c lattice parameters, along with a reduced unit cell volume, may be attributed to lattice strain, surface stress, or defect incorporation such as oxygen vacancies introduced during the synthesis process. Additionally, interactions with phytochemicals present in the *Justicia adhatoda* extract may influence the nucleation and growth of ZnO crystals, leading to minor structural distortions.

3.2 UV-visible absorption analysis

UV-Vis spectroscopy was employed to investigate the optical properties of ZnO NPs synthesized using *J. adhatoda* leaf extract. The absorption spectrum, depicted in Fig. 3, reveals a prominent absorption peak at approximately 371 nm. This band-edge absorption is a hallmark of ZnO's electronic structure and provides valuable insights into the particle size, crystallinity, and defect states of the synthesized NPs. Compared to bulk ZnO, which typically exhibits a band-edge absorption around 375 nm, the observed absorption peak at 371 nm indicates a slight blue-shift of ~4 nm.

This shift is relatively moderate compared to previously reported values, where ZnO NPs synthesized using *J. adhatoda* extract have shown blue shifts up to 353 nm.[34] The limited blue-shift in this study suggests that the synthesized ZnO NPs possess a size distribution that is not significantly confined to the quantum regime, where the quantum confinement effect dominates, but still exhibits a reduction in size compared to bulk ZnO. The blue shift may be attributed to the reduction in particle size, leading to an increased bandgap energy, as well as potential variations in defect states within the ZnO matrix.

The presence of phytochemicals in *J. adhatoda* extract plays a crucial role in the synthesis process, acting as both reducing and capping agents. Bioactive compounds such as flavonoids, alkaloids, and terpenoids contribute to the stabilization of ZnO NPs by minimizing surface defects and preventing agglomeration. The sharpness and intensity of the absorption peak further confirm the monodispersity and high crystallinity of the synthesized ZnO NPs, indicating effective phytochemical-assisted synthesis. Interestingly, the band-edge position suggests that the ZnO NPs synthesized in this study contain a moderate density of oxygen-related defects, which has also been reported in earlier studies where bandgap narrowing and band-edge shifts were attributed to oxygen vacancies and surface defects in ZnO NPs.[35] Oxygen vacancies and interstitial defects within the ZnO lattice can introduce localized states within the bandgap, subtly modifying the optical absorption characteristics. The smaller blue-shift, compared to other reported ZnO NPs synthesized with *J. adhatoda*, could be attributed to differences in synthesis parameters, including reaction temperature, pH, reaction time, and extract concentration, which influence defect formation and particle growth.

Overall, the UV-Vis absorption analysis highlights the successful green synthesis of ZnO NPs using *J. adhatoda* extract,

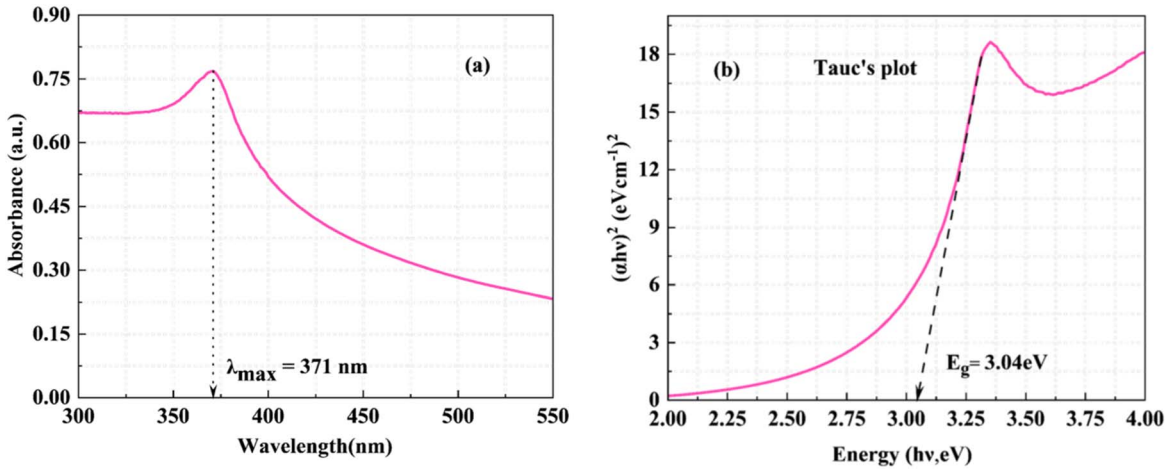

Fig. 3 UV-vis spectra (a) and (b) Tauc plot for energy band gap analysis of *J. adhatoda*/ZnO NPs.

demonstrating the potential of phytochemical-mediated approaches for controlling nanoparticle properties. The 371 nm absorption peak signifies a balance between size confinement and defect-state formation, ensuring that the ZnO NPs retain desirable optical and electronic properties for potential applications in photocatalysis.

Green synthesis of ZnO NPs using different plant extracts has shown considerable variations in optical properties, particularly in absorption peaks and bandgap energies. These differences arise due to the distinct phytochemical compositions of plant extracts, which influence the nucleation, growth, and surface capping of the nanoparticles. The absorption peaks of ZnO NPs from different plant extracts range between 326 nm and 445 nm, while the corresponding bandgap energies vary from 2.66 eV to 3.73 eV from Table 4. These variations can significantly affect the material's applicability in photocatalysis, optoelectronics, and biomedical applications. ZnO NPs synthesized using *Epipremnum aureum* exhibited an absorption peak at 326 nm with the highest reported bandgap of 3.73 eV,[36] suggesting strong quantum confinement effects and small particle sizes. Conversely, *Carica papaya*-mediated ZnO NPs demonstrated the lowest bandgap energy of 2.88 eV with an absorption peak at 375 nm,[37] indicating the presence of larger nanoparticles or increased defect density that facilitates lower-energy electronic transitions. Similarly, *Lupinus albus*-derived ZnO NPs displayed an absorption peak at 357 nm with a bandgap of 3.25 eV,[38] positioning them within the mid-range of reported values. A distinct trend is observed in *Allium cepa*-mediated ZnO NPs, which show long absorption peaks at 445 nm, with corresponding bandgap energies of 2.66–2.69 eV.[39] Similarly, *Pelargonium odoratissimum*-based ZnO NPs exhibited absorption peaks around 370 nm, 3.28 eV.[40] For ZnO NPs synthesized using *Justicia adhatoda*, multiple studies have reported varying results. Previous works have recorded absorption peaks at 353 nm, with bandgap energies of 3.09.[7] The present study, however, reports an absorption peak at 371 nm with a bandgap of 3.04 eV, indicating a slight redshift compared to earlier findings. This shift suggests differences in synthesis conditions, phytochemical interactions, or nanoparticle aggregation, which could influence electronic properties. The comparatively lower bandgap of 3.04 eV in this study implies enhanced visible light absorption, making the synthesized ZnO NPs potentially more effective in photocatalytic and optoelectronic applications. The variations observed across different plant-mediated ZnO NPs highlight the importance of phytochemical-assisted synthesis in controlling the structural and optical properties of nanoparticles, emphasizing the significance of green synthesis as a tunable and eco-friendly approach to nanomaterial development.

3.3 FTIR analysis

The FTIR spectrum of *J. adhatoda* leaf extract Fig. 4(a) highlights the key functional groups responsible for its biochemical properties and potential role in ZnO nanoparticle synthesis. The

Table 4 Comparative study of *J. adhatoda*/ZnO NPs with different plant extracts ZnO NPs: absorption peaks and bandgap energies

S. no	Plant extract used	Absorption peak (nm)	Band gap energy (eV)	References
1	*Epipremnum aureum*	326	3.73	36
2	*Carica papaya*	375	2.88	37
3	*Lupinus albus*	357	3.25	38
4	*Allium cepa*	445	2.66–2.69	39
5	*Pelargonium odoratissimum*	370	3.28	40
6	*Justicia adhatoda*	353	3.09	7

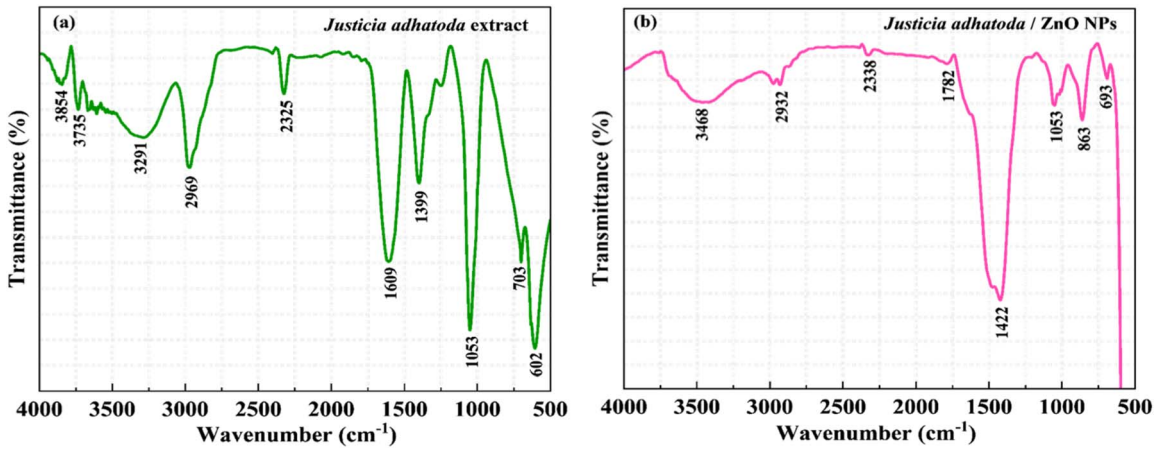

Fig. 4 FTIR spectrum: (a) *J. adhatoda* extract and (b) *J. adhatoda*/ZnO NPs.

peaks at 3854 cm^{-1} and 3735 cm^{-1} correspond to O–H stretching vibrations, indicating the presence of hydroxyl groups from phenolic compounds or alcohols. A distinct band at 3291 cm^{-1} is associated with N–H stretching, suggesting the presence of amines or amides, which could be involved in the interaction with metal ions during nanoparticle formation.

The absorption at 2969 cm^{-1} corresponds to C–H stretching, typically found in alkanes, hinting at the presence of lipid or hydrocarbon-containing phytochemicals. A notable peak at 2325 cm^{-1} signifies C≡N stretching, pointing to nitrile groups, while the strong band at 1609 cm^{-1} is indicative of C=O stretching, likely arising from ketones, aldehydes, or carboxyl compounds. The peak at 1399 cm^{-1} is linked to O–H bending, reinforcing the presence of hydroxyl-rich biomolecules. In the lower wavenumber region, the peak at 1053 cm^{-1} corresponds to C–O stretching, which may be attributed to polysaccharides, ethers, or ester linkages from plant metabolites. The bands at 703 cm^{-1} and 602 cm^{-1} suggest C–C stretching or aromatic ring vibrations, confirming the presence of complex organic structures. These phytochemical constituents, including flavonoids, alkaloids, and terpenoids, play a crucial role in the reduction and stabilization process of ZnO nanoparticles in green synthesis.

The FTIR spectrum of the green-synthesized *J. Adhatoda*/ZnO NPs Fig. 4(b) reveals significant peaks that confirm the successful formation of nanoparticles and the interaction of phytochemicals with the ZnO surface. The broad absorption band at 3468 cm^{-1} corresponds to the O–H stretching vibration, indicating the presence of hydroxyl groups from phenols or alcohols, which play a crucial role in nanoparticle stabilization. The peak at 2932 cm^{-1} is attributed to C–H stretching, suggesting the presence of aliphatic compounds from organic biomolecules. A distinct peak at 2338 cm^{-1} is associated with C≡N stretching, indicating the presence of nitrile-containing compounds, while the band at 1782 cm^{-1} corresponds to C=O stretching, confirming the presence of carbonyl groups from carboxylic acids, esters, or ketones. Additionally, the peak at 1422 cm^{-1} can be assigned to C–N stretching or O–H bending, highlighting the involvement of amines or phenolic compounds in the synthesis process.[41,42] The sharp band at 1053 cm^{-1} corresponds to C–O stretching vibrations, suggesting the presence of alcohols, ethers, or polysaccharides from plant-derived phytochemicals. The peak at 863 cm^{-1} could be attributed to out-of-plane bending vibrations of aromatic compounds, indicating the role of flavonoids or other aromatic structures in the nanoparticle formation. Finally, the characteristic peak at 693 cm^{-1} corresponds to Zn–O stretching, confirming the effective synthesis of ZnO nanoparticles.

These findings suggest that bioactive compounds from the plant extract acted as reducing and stabilizing agents, facilitating the green synthesis of ZnO NPs. The findings support existing research, demonstrating that alkaloids and flavonoids in *J. adhatoda* facilitate nanoparticle formation by acting as natural stabilizers. Applications in photocatalysis, antimicrobial therapies, and environmental restoration are anticipated for these ZnO NPs, produced *via* a green and biocompatible synthesis route. FTIR analysis demonstrates the significance of phytochemicals in nanoparticle generation and verifies their structural stability.

3.4 FESEM analysis

The surface morphology and elemental composition of *J. adhatoda*/ZnO NPs were examined using scanning electron microscopy (SEM) at different magnifications. The SEM images provide valuable insights into the particle shape, aggregation behavior, and porosity of the synthesized material.

The SEM micrograph at 20k× magnification Fig. 5(a) displays a highly aggregated nanoparticle structure, where the ZnO NPs appear to form interconnected clusters. At 40k× magnification Fig. 5(b), the individual nanoparticles become more distinguishable, revealing that the particles are mostly flaky and irregularly shaped, with some exhibiting plate-like and flower-like morphologies.[43,44] This structural diversity is characteristic of green-synthesized ZnO NPs due to the influence of phytochemical compounds from *J. adhatoda* leaf extract, which act as both reducing and stabilizing agents. The presence of sheet-like and rough-edged nanoparticles suggests that

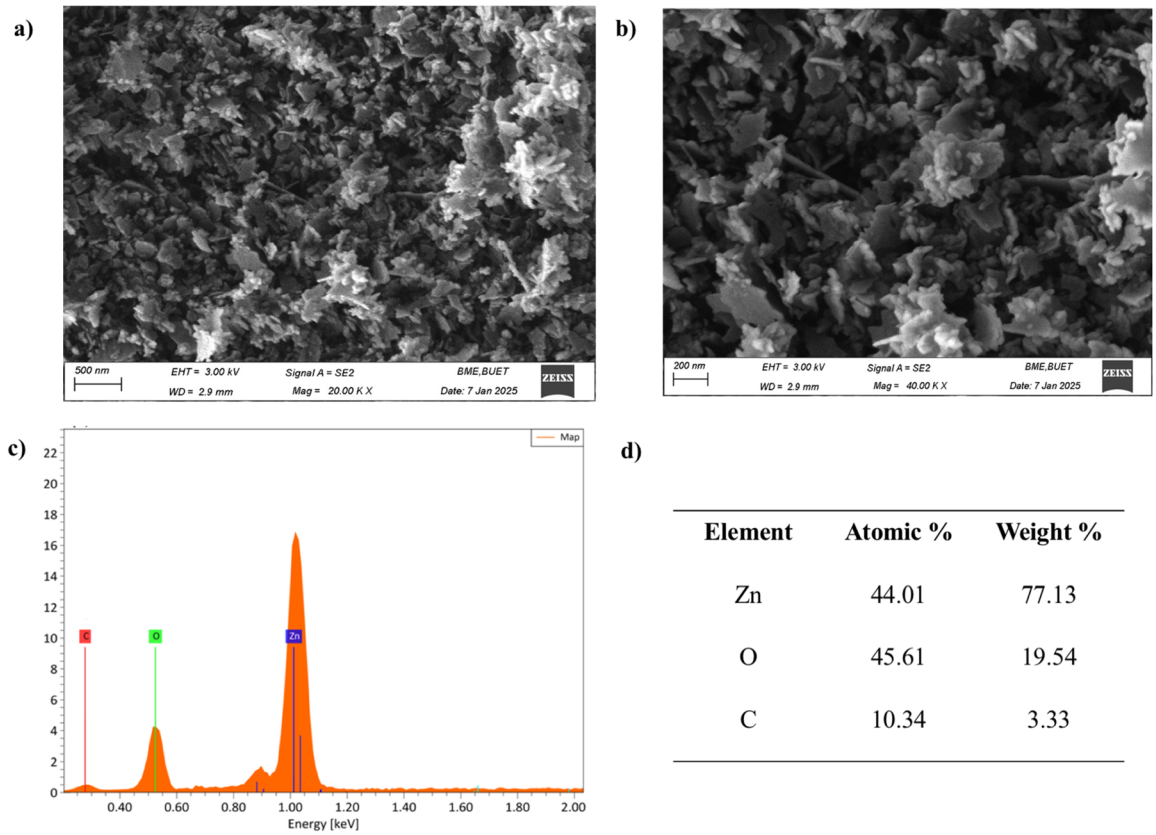

Element	Atomic %	Weight %
Zn	44.01	77.13
O	45.61	19.54
C	10.34	3.33

Fig. 5 SEM micrographs of (a and b), *J. adhatoda*/ZnO NPs at varying magnifications, mentioning their agglomerated nanostructure, (c) EDX analysis, and (d) weight and atomic percentages of Zn, O and C.

nucleation and growth mechanisms were significantly influenced by bioactive compounds, leading to the formation of hierarchical nanostructures. Unlike chemically synthesized ZnO NPs, which often show well-defined spherical or rod-like structures, the biogenic synthesis process results in nanosheets and nanoaggregates with irregular, jagged edges. This morphology likely contributes to a larger surface area and improved functional properties, making the nanoparticles particularly advantageous for photocatalytic applications.

A closer examination of the SEM images indicates that the ZnO NPs possess a rough flower-like structure. The aggregation of the particles creates micro- and nano-scale voids between them, leading to an intrinsic porous architecture. The presence of nanoscale gaps and interconnected voids within the ZnO NP clusters suggests that these materials have high surface area and porosity, which are beneficial for catalytic and adsorption applications. The porous structure can be attributed to the role of plant-based organic compounds during the synthesis process. Phytochemicals present in the *J. adhatoda* extract likely act as capping agents, preventing excessive crystal growth while promoting the formation of a rough, textured surface. These structural features enhance the material's ability to adsorb reactants, making it highly suitable for applications such as pollutant degradation, gas sensing, and biomedical uses.

The observed hierarchical aggregation and nanoscale voids contribute to an increased surface area, enhancing their potential for applications in photocatalysis, adsorption, antibacterial treatments, and energy storage. The bioactive compounds present in the leaf extract influence the nucleation and growth of the ZnO NPs, preventing excessive crystallization and promoting structural diversity, which is rarely achieved in conventional chemical synthesis. The structural advantages of these ZnO NPs make them highly effective in the photocatalytic degradation of pollutants, where their rough surfaces and high porosity facilitate greater light absorption and ROS generation. Their porous architecture also enhances adsorption capacity, making them suitable for environmental remediation, particularly for removing heavy metals and dyes from wastewater.

The elemental composition of the synthesized ZnO NPs was examined using Energy Dispersive X-ray Spectroscopy (EDX). The EDX spectrum Fig. 5(c) confirms the presence of zinc (Zn), oxygen (O), and carbon (C) as the primary constituents, verifying the successful formation of ZnO NPs. The characteristic peaks for Zn appear at approximately the K-α line at 1.01 keV, while the oxygen peak is observed at the K-α line at 0.52 keV. Additionally, a peak corresponding to carbon is detected around the K-α line at 0.28 keV. The percentage of weight present under the irradiated area is 77.13%, 19.54%, and 3.33% for zinc, oxygen, and carbon, respectively, for green-synthesized ZnO NPs Fig. 5(d). The presence of carbon is from the plant extract components existing in the NPs surface (also shown in FTIR data) or carbon tape from the sample holder. A similar result has been found in the literature.[41]

4. Photocatalytic activity evaluation

4.1 Dye degradation

Methylene blue dye was used in the experiment to evaluate the photocatalytic efficiency of the synthesized *J. adhatoda*/ZnO NPs as photocatalyst under solar irradiation. The degradation process was further optimized by varying the photocatalyst dosage, exposure time, initial dye concentration, and pH value to achieve maximum dye breakdown.

4.1.1 Effect of catalyst dosage on dye degradation. The consequence of photocatalysts dose on MB degradation using ZnO NPs is depicted in the figure. By altering the quantity of photocatalysts from 10, 20, 30, 40, 50, and 60 mg while maintaining a fixed MB concentration of 10 mg L^{-1}, dye solution natural pH, and irradiation period of 120 minutes, the impact of catalyst dose was investigated. According to the data shown in the Fig. 6, all samples' MB degradation rises significantly when the catalyst dosage is raised from 10 mg to 50 mg. Nevertheless, the rate of removal of color decreased when the catalyst dosage was escalated over 50 mg (98.13%).

The commonly accepted reason for this result is that by increasing the addition of active agents leads to a greater number of active sites. on the catalyst's surface. Thus, 50 mg of ZnO photocatalysts results in the greatest decolonization of MB. Raising the catalyst quantity beyond 50 mg unexpectedly caused a reduction in the degradation efficiency, reaching 95.71% at a 60 mg dose. This counterintuitive result suggests that at higher concentrations, the catalyst particles may aggregate, forming larger clusters. These larger clusters can limit the accessibility of active sites on the catalyst's surface, hindering the interaction with the target molecules and thus reducing the overall reaction efficiency. This phenomenon underscores the significance of fine-tuning catalyst dosage for optimal degradation performance rates while avoiding self-deactivation through aggregation.[45] Additionally, an excessive amount of catalyst can cause scattering influencing the clarity of the solution, which in turn reduces the surface area of the catalyst exposed to light and hampers its photocatalytic efficiency.[46] The plots of reaction rate kinetics revealed that the rate of the reaction is improved constantly by escalating the catalyst dosages until a certain level of optimization.

4.1.2 Effect of dye concentration. Additionally, varied MB concentrations of 10, 20, 30, and 40 ppm were utilized to assess the effectiveness of the green produced ZnO NPs, although the concentrations of nanocatalysts, pH, and irradiation period remained persistent at 50 mg, natural dye pH, and 120 minutes respectively. The Fig. 7 illustrates how the original dye concentration affects MB's decolonization. The findings showed that when the dye's initial concentration increases, MB's degradation efficiency falls. At low concentrations, maximum degradation was attained. Therefore, it was discovered that MB was best removed at low concentrations, namely 10 ppm. The results showing in the Fig. 7 that increasing the concentration of MB from 10 to 40 ppm leads in a reduction in MB breakdown. While they showed a decrease at higher dye concentrations, the decomposition rate and rate photodegradation constant improved at reduced dye concentrations. The effectiveness of the photocatalytic process depends on the extent to which light penetrates the solution and interacts with the ZnO NPs, thereby enhancing the reduction of absorbed oxygen.[47] The incoming light can absorb the color solution from the photocatalyst and saturate it at lower dye concentrations. The amount of hydroxyl radicals and superoxide ions $(OH/O_2^{\bullet})$ generated at the photocatalyst's surface determines the pace of degradation, therefore increasing the number of dye molecules may block active sites and lessen the light's influence on these sites for the creation of $OH^{\bullet}$.

High dye concentrations might cause a considerable quantity of light to be incorporated into the dye molecular system instead of the photocatalysts, which lowers the production of superoxide ions $(O_2^{\bullet -})$ and hydroxyl radicals $(OH^{\bullet})$.[48] As a result, the limited concentration of free radicals was insufficient to counteract the growing number of MB dye molecules as their concentration increased. Moreover, the solution's color

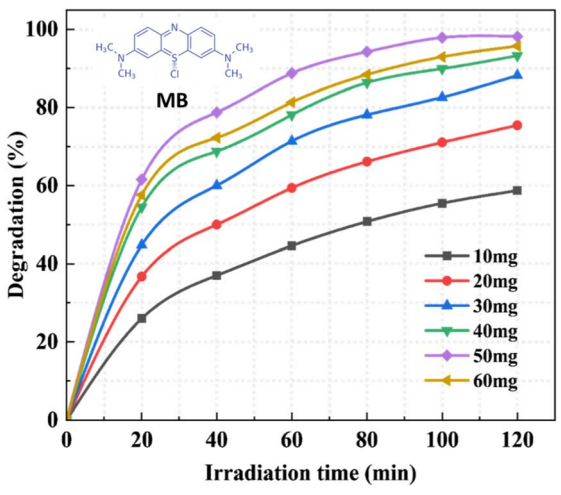

Fig. 6 Effect of *J. adhatoda*/ZnO NPs dose on MB dye degradation.

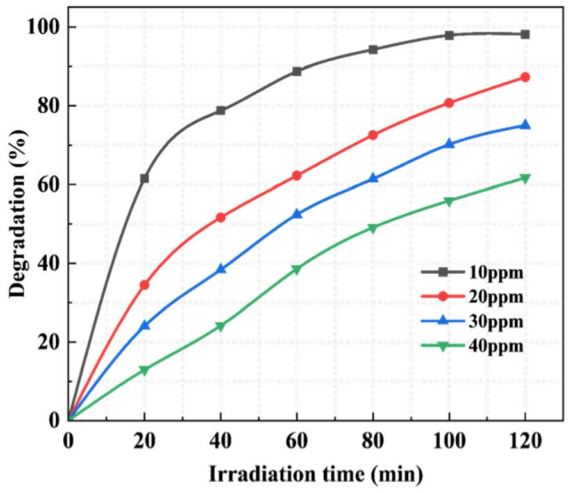

Fig. 7 Effect of concentration of MB on dye degradation by *J. adhatoda*/ZnO NPs.

intensified with higher dye concentrations. Thus, the reaction rate decreased.

4.1.3 Effect of pH on dye degradation. The Fig. 8, illustrates that how pH affects the removal of methylene blue for ZnO NPs. The performance of metal oxide photocatalysts is significantly influenced by the pH of the MB solution, as it affects their surface charge. This study used four different pH levels of MB solution (5, 7, 9, 11) to improve dye solution pH while maintaining constant catalyst dosage (50 mg), dye concentration (10 ppm), and irradiation period (120 minutes). The study found that increasing the pH level significantly improved breakdown efficiency. At pH 5, MB degradation was 55.35%, but increased to 75.24%, 91.37%, and 99.12% at pH 7, 9, and 11, respectively (Fig. 10). Increasing the pH from 5 to 11 led to higher degradation of the MB dye. Photocatalyst surfaces possess a negative charge in basic environments and a positive charge in acidic ones. As a cationic dye, MB's structure becomes positively charged when dissolved in water. In alkaline conditions, MB breaks down more rapidly because of enhanced interactions between opposite charges between the solution and the nanocomposite surface.[49] This data highlights the exceptional performance of the photocatalyst under basic conditions. The enhanced decolonization observed at higher pH can be ascribed to the electrostatic attraction between positively charged MB molecules and the negatively charged surface of ZnO NPs. This favorable basic environment promotes the adsorption of contaminant ions onto the catalytic surface. The reduced degradation rate at neutral pH was attributed to the proximity of the zero-point charge (pH_{zpc}) region, where zinc oxide nanoparticles tend to aggregate. This aggregation diminishes the generation of hydroxyl radicals ($OH^{\bullet}$), leading to a lower degradation efficiency.[50]

4.1.4 Kinetic study of MB dye degradation. The kinetics of dye degradation were investigated using *J. adhatoda*/ZnO NPs at a photocatalyst dose of 50 mg and a dye concentration of 10 ppm under alkaline conditions (pH 11). Fig. 9. represents the degradation process was analyzed using pseudo-zero-order, pseudo-first-order, and pseudo-second-order kinetic models to determine the most suitable reaction order (Table 5). Based on the regression coefficients (R^2 values), the pseudo-first-order model provided the best fit for the degradation data, with an R^2 value of 0.98. This suggests that the degradation rate is primarily influenced by the concentration of the remaining dye molecules. The calculated rate constant (k_1) for the pseudo-first-order model was 0.037 min^{-1}, indicating a relatively rapid degradation process under the given conditions.

Comparatively, the pseudo-zero-order model exhibited a lower R^2 value of 0.76 with a rate constant (k_0) of −0.013 mg L^{-1} min^{-1}, while the pseudo-second-order model showed the poorest correlation ($R^2 = 0.61$) with a rate constant (k_2) of 0.382 L mg^{-1} min^{-1} depicted in Table 5. The lower regression coefficients for these models indicate they are less appropriate for describing the reaction kinetics in this system. The observed increase in the pseudo-first-order rate constant with a higher catalyst dosage highlights the positive correlation between ZnO NP concentration and the degradation rate. This behavior aligns with the enhanced generation of reactive oxygen species (ROS) at elevated catalyst concentrations, contributing to improved dye degradation efficiency. Furthermore, the ability of *J. adhatoda*/ZnO NPs to maintain a high removal efficiency across multiple reuse cycles emphasizes their stability and potential for sustainable wastewater treatment applications.

4.1.5 Degradation mechanism. Fig. 10 shows the schematic diagram of the proposed mechanism of photocatalytic activity of biosynthesized *J. adhatoda*/ZnO NPs against MB dye. The photocatalytic degradation of methylene blue (MB) by ZnO nanoparticles proceeds through light-induced electron–hole pair generation, charge transfer, and reactive oxygen species (ROS) formation. Upon sunlight irradiation, ZnO absorbs photons with energy greater than or equal to its band gap (3.04 eV), exciting electrons from the valence band (VB) to the conduction band (CB), leaving behind holes in the VB (eqn (4)). Similar radical-based mechanisms have been reported in recent studies.[1] ZnO NPs undergo photoexcitation, generating electron–hole pairs within the semiconductor under sunlight exposure. Maximizing photocatalytic efficiency necessitates minimizing the recombination of these charge carriers, as the effectiveness of the process hinges on the interaction between generated holes and electron acceptors, and between electrons and electron donors. Photogenerated holes can oxidize water and hydroxyl ions, leading to the formation of highly reactive hydroxyl radicals ($OH^{\bullet}$). Simultaneously, photogenerated electrons interact with oxygen to produce superoxide radicals ($O_2^{\bullet}$). These superoxide radicals can subsequently protonate in the aqueous medium, forming hydroperoxyl radicals ($HO_2^{\bullet}$), which can further transform into hydrogen peroxide (H_2O_2). The generated hydrogen peroxide can then dissociate into more reactive $OH^{\bullet}$ radicals. The generated $^{\bullet}OH$ radicals, along with superoxide radicals ($O_2^{\bullet}$) and hydroperoxy radicals ($HO_2^{\bullet}$), act as potent oxidants, driving the degradation of contaminants. This oxidative action ultimately transforms the dye into harmless end products, such as carbon dioxide and water, through a series of redox reactions. The produced ($OH^{\bullet}$), ($HO_2^{\bullet}$), and ($O_2^{\bullet}$)

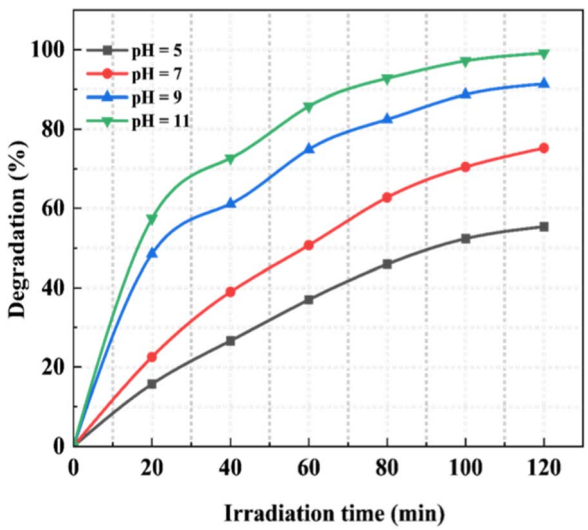

Fig. 8 Effect of pH on MB dye degradation by *J. adhatoda*/ZnO NPs.

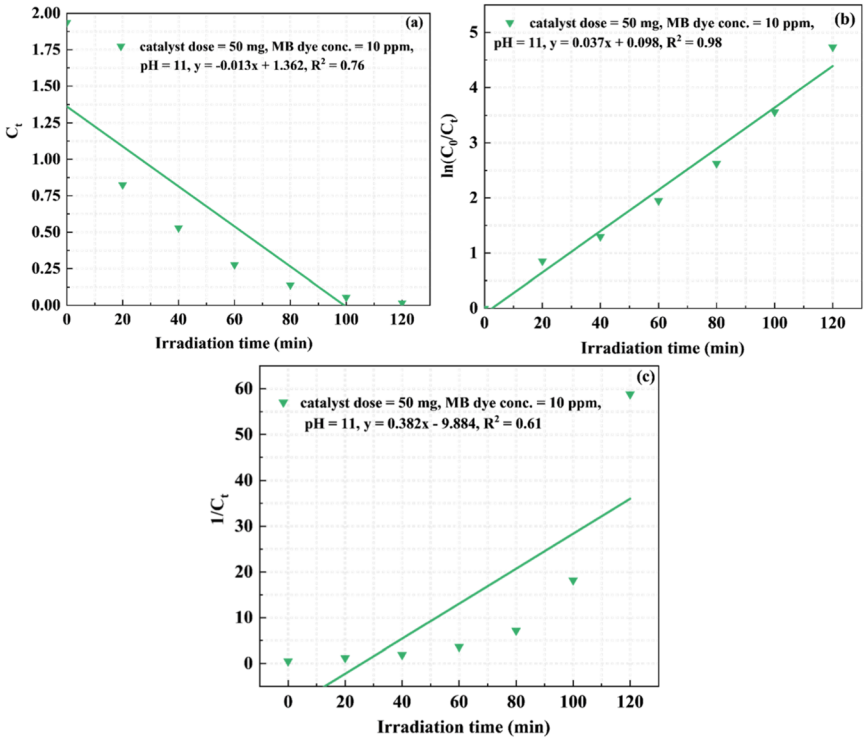

Fig. 9 Kinetics study of degradation of MB dye: (a) pseudo-zero-order, (b) pseudo-first-order and (c) pseudo-second-order.

Table 5 Calculated rate constants for dye degradation reactions using different kinetic models

Photocatalyst-dose (mg)	Dye conc. (ppm)	pH	% Removal	Pseudo-zero-order		Pseudo-first-order		Pseudo-second-order	
				k_0 (mg L^{-1} min^{-1})	R^2	k_1 (min^{-1})	R^2	k_2 (L mg^{-1} min^{-1})	R^2
50	10	11	99.12	−0.013	0.76	0.037	0.98	0.382	0.61

radicals are potent oxidizing agents responsible for breaking down pollutants, facilitating the transformation of the dye into non-toxic substances like carbon dioxide and water.[51–55] The fundamental steps in the process of photocatalysis are listed as followed by-

$$ZnO + h\nu \rightarrow ZnO\ (e_{CB}^- + h_{VB}^+) \quad (4)$$

$$O_2 + e_{CB}^- \rightarrow O_2^{\bullet -} \quad (5)$$

$$O_2^{\bullet -} + H^+ \rightarrow HO_2^{\bullet} \quad (6)$$

$$HO_2^{\bullet} + HO_2^{\bullet} \rightarrow H_2O_2 + O_2 \quad (7)$$

$$H_2O_2 + O_2^{\bullet -} \rightarrow OH^{\bullet} + OH + O_2 \quad (8)$$

$$O_2^{\bullet -} + HO_2^{\bullet} \rightarrow HO_2^- + O_2 \quad (9)$$

$$HO_2 + H^+ \rightarrow H_2O_2 \quad (10)$$

$$H_2O_2 + h\nu \rightarrow 2OH^{\bullet} \quad (11)$$

$$H_2O_2 + e^- \rightarrow OH^{\bullet} + OH^- \quad (12)$$

$$H_2O + h_{VB}^+ \rightarrow OH^{\bullet} + H^+ \quad (13)$$

$$OH^- + h_{VB}^+ \rightarrow OH^{\bullet} \quad (14)$$

$$ROS\ (OH^{\bullet}, O_2^{\bullet -}, h^+) + MB\ dye \rightarrow degradation\ products\ (CO_2 + H_2O) \quad (15)$$

5. Perspective for future work

Although the present study demonstrates the effectiveness of *J. adhatoda*-mediated ZnO nanoparticles in the photocatalytic degradation of methylene blue, several areas remain open for further exploration. Future studies should focus on the following aspects:

(1) Advanced characterizations: incorporating techniques such as photocurrent response measurements and electrochemical impedance spectroscopy (EIS) will provide deeper insights into charge carrier separation, mobility, and recombination resistance, thus strengthening the mechanistic understanding.

(2) Band structure and defect analysis: complementary approaches such as Mott–Schottky (M–S) plots,

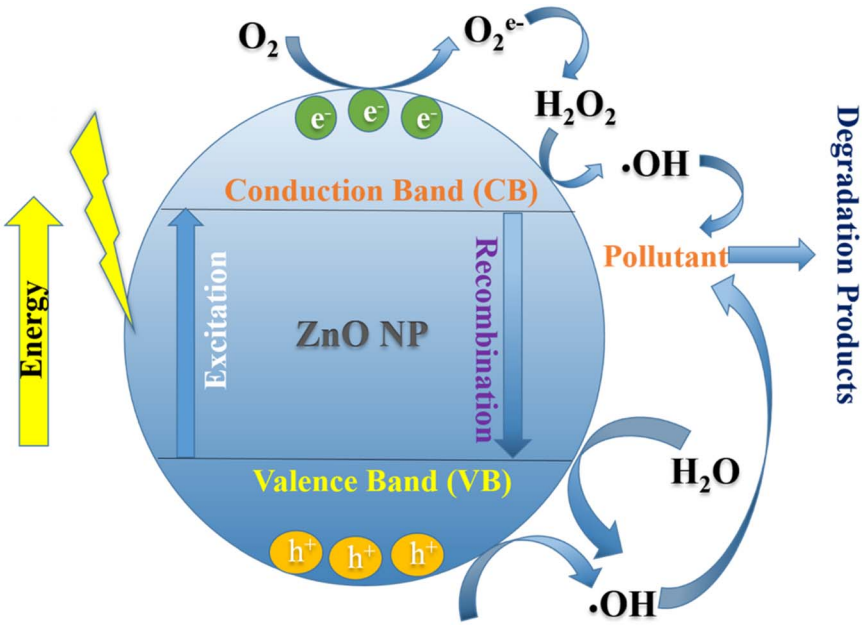

Fig. 10 *J. adhatoda*/ZnO NPs mechanism in photocatalytic degradation of MB dye.

photoluminescence (PL), and density functional theory (DFT) calculations could be used to clarify the band structure, defect states, and electronic properties that govern photocatalytic behavior.

(3) Mechanism elucidation – a more detailed investigation of reactive oxygen species (ROS) using scavenger studies or electron spin resonance (ESR) spectroscopy will help to directly confirm the roles of $^{\bullet}OH$, $^{\bullet}O_2^-$, and h^+ species in pollutant degradation. Additionally, the degradation pathway of methylene blue and possible intermediate products could be tracked using LC-MS or HPLC analysis.

(4) Stability and reusability – long-term performance tests with multiple reuse cycles are necessary to evaluate catalyst durability, which is critical for practical applications.

6. Conclusion

ZnO NPs were successfully synthesized using an eco-friendly and cost-effective method. The resulting nanoparticles were characterized by UV-Vis, FTIR, XRD, SEM, and EDX analyses. The *J. adhatoda*-mediated ZnO NPs followed pseudo-first-order kinetics, achieving a relatively high rate constant of 0.037 min^{-1} for methylene blue degradation under sunlight. This enhanced photocatalytic activity can be attributed to their small crystallite size, high crystallinity, reduced band gap energy, and multi-structured morphology. Investigating the best conditions for methylene blue dye removal revealed that increasing the dye concentration without simultaneously increasing the number of ZnO NPs reduced removal performance. A better removal efficiency was achieved, however, by increasing the amount of ZnO NPs, which increased the number of active sites and interactions between the adsorbate and adsorbent. The elimination efficiency was 99.12% with 50 mg of ZnO NPs. The degradation % stabilized and the adsorption process reached equilibrium after 120 min of irradiation. Higher pH levels resulted in greater removal effectiveness of methylene blue because, being a cationic dye, the electrostatic interaction between the dye and ZnO NPs increased with pH. Importantly, this study highlights the green perspective of the developed technique. The synthesis utilized a plant extract as a natural reducing and stabilizing agent, avoided toxic chemicals, and employed solar energy as a renewable light source, thereby minimizing secondary pollution and operational costs. These aspects align well with the principles of green chemistry and sustainable wastewater treatment. Such eco-friendly nano photocatalysts provide a promising route for the degradation of dyes and other organic contaminants, supporting the development of safer and scalable water purification technologies.

Conflicts of interest

There are no conflicts to declare.

Data availability

The data that support the findings of this study are available from the corresponding author upon reasonable request.

References

1 F. H. Abdullah, N. H. H. Abu Bakar and M. Abu Bakar, *J. Hazard. Mater.*, 2021, **406**, 124779.
2 M. Kumar, A. K. P. Venugopal and K. Pakshirajan, *Environ. Sci. Pollut. Res.*, 2022, **29**, 38478–38492.
3 M. Arami, N. Y. Limaee, N. M. Mahmoodi and N. S. Tabrizi, *J. Colloid Interface Sci.*, 2005, **288**, 371–376.

4 W. Artifon, K. Cesca, C. J. De Andrade, A. A. Ulson De Souza and D. De Oliveira, *Process Biochem.*, 2021, **111**, 181–190.
5 D. Jalandhara, S. Kumar, J. Dalal, Supreet, G. Singh, S. Kumar, R. Badru, Y. Singh, S. V. Sharma and S. Kaushal, *Mater. Adv.*, 2025, **6**, 641–657.
6 A. Khan, P. Ju, Z. Han and C. Ni, *Aqua Water Infrastruct. Ecosyst. Soc.*, 2024, **73**, 266–285.
7 M. Mahajan, S. Kumar, J. Gaur, S. Kaushal, J. Dalal, G. Singh, M. Misra and D. S. Ahlawat, *RSC Adv.*, 2025, **15**, 2958–2980.
8 S. Rohilla, A. Gupta, V. Kumar, S. Kumari, M. Petru, N. Amor, M. T. Noman and J. Dalal, *Nanomaterials*, 2021, **11**, 2548.
9 W. Xie, G. Liu, Y. Liu, Y. Bai, Y. Liao, T. Li, C. Wang, S. Chang and J. Hu, *J. Porous Mater.*, 2024, **31**, 1655–1681.
10 Y. Deng and R. Zhao, *Curr. Pollut. Rep.*, 2015, **1**, 167–176.
11 A. Suguna, S. Prabhu, R. Siranjeevi, S. Pugazhendhi and C. Sridevi, *J. Mater. Sci. Mater. Electron.*, 2023, **34**, 1655.
12 A. K. Shimi, C. Parvathiraj, S. Kumari, J. Dalal, V. Kumar, S. M. Wabaidur and Z. A. Alothman, *Environ. Sci. Adv.*, 2022, **1**, 849–861.
13 J. Gaur, S. Kumar, M. Pal, H. Kaur, K. M. Batoo, J. O. Momoh and Supreet, *Hybrid Adv.*, 2024, **5**, 100128.
14 D. A. De Souza, P. H. D. A. Da Silva, F. P. Da Silva, Y. Romaguera-Barcelay, R. D. Ferreira, E. A. Araujo Junior, J. F. D. L. Nascimento, F. F. Da Costa, L. L. Takeno, Y. Leyet Ruiz, L. A. Dominguez, W. R. Brito and F. X. Nobre, *Colorants*, 2024, **3**, 229–252.
15 Q. Zhang, X. Zhao, L. Duan, H. Shen and R. Liu, *J. Photochem. Photobiol. Chem.*, 2020, **392**, 112156.
16 K. C. Paradva, R. Jangir and S. Kalla, *Inorg. Chem. Commun.*, 2023, **158**, 111584.
17 M. Y. Al-darwesh, S. S. Ibrahim and M. A. Mohammed, *Results Chem.*, 2024, **7**, 101368.
18 A. Nyabadza, É. McCarthy, M. Makhesana, S. Heidarinassab, A. Plouze, M. Vazquez and D. Brabazon, *Adv. Colloid Interface Sci.*, 2023, **321**, 103010.
19 N. S. Alsaiari, F. M. Alzahrani, A. Amari, H. Osman, H. N. Harharah, N. Elboughdiri and M. A. Tahoon, *Molecules*, 2023, **28**, 463.
20 N. Rani, S. Yadav, A. Mushtaq, S. Rani, M. Saini, S. Rawat, K. Gupta, K. Saini and D. Maity, *Chem. Pap.*, 2024, **78**, 3687–3704.
21 N. Govindan, K. Vairaprakasam, C. Chinnasamy, T. Sivalingam and M. K. A. Mohammed, *Mater. Adv.*, 2020, **1**, 3460–3465.
22 C. Wu, T. Zhang, B. Ji, Y. Chou and X. Du, *Cellulose*, 2024, **31**, 4849–4864.
23 S. Faisal, H. Jan, S. A. Shah, S. Shah, A. Khan, M. T. Akbar, M. Rizwan, F. Jan, Wajidullah, N. Akhtar, A. Khattak and S. Syed, *ACS Omega*, 2021, **6**, 9709–9722.
24 J. Arumugam, S. Thambidurai, S. Suresh, M. Selvapandiyan, M. Kandasamy, N. Pugazhenthiran, S. Karthick Kumar, T. Muneeswaran and F. Quero, *Chem. Phys. Lett.*, 2021, **783**, 139040.
25 K. Singh, J. Singh and M. Rawat, *SN Appl. Sci.*, 2019, **1**, 624.
26 M. Selvaraj, N. Hema and V. Parthasarathy, *BioNanoScience*, 2020, **10**, 112–121.
27 D. Latha, S. Sampurnam, C. Arulvasu, P. Prabu, K. Govindaraju and V. Narayanan, *Mater. Today Proc.*, 2018, **5**, 8968–8972.
28 M. Nasir, R. Ramash, H. Fatima, S. Ashraf, I. Munir, S. Asghar, M. Adnan, A. Masood and S. K. Chaudhari, *Scientifica*, 2024, **2024**, 1374346.
29 M. Rudrapal, S. Vallinayagam, S. Aldosari, J. Khan, H. Albadrani, A. Al-Shareeda and M. Kamal, *Front. Nutr.*, 2023, **10**, 1161471.
30 C. D. M. Strieder, D. L. P. Macuvele, C. Soares, N. Padoin and H. G. Riella, *J. Mater. Res. Technol.*, 2024, **30**, 6376–6388.
31 M. Ramzan, F. Ayub, A. A. Shah, G. Naz, A. N. Shah, A. Malik, R. Sardar, A. Telesiński, H. M. Kalaji, E. S. Dessoky and H. A. Elgawad, *Front. Plant Sci.*, 2022, **13**, 900347.
32 J. Wojnarowicz, T. Chudoba and W. Lojkowski, *Nanomaterials*, 2020, **10**, 1086.
33 M. H. Kalaba, S. A. Moghannem, A. S. El-Hawary, A. A. Radwan, M. H. Sharaf and A. S. Shaban, *Plants*, 2021, **10**, 1760.
34 M. K. Debanath and S. Karmakar, *Mater. Lett.*, 2013, **111**, 116–119.
35 J. Wang, P. Liu, X. Fu, Z. Li, W. Han and X. Wang, *Langmuir*, 2009, **25**, 1218–1223.
36 R. S. Brishti, M. Ahsan Habib, M. H. Ara, K. M. Rezaul Karim, M. Khairul Islam, J. Naime, M. M. Hasan Rumon and M. A. Rayhan Khan, *Results Chem.*, 2024, **7**, 101441.
37 J. Gaur, K. Vikrant, K.-H. Kim, S. Kumar, M. Pal, R. Badru, S. Masand and J. Momoh, *Mater. Today Sustainability*, 2023, **22**, 100339.
38 A. Muhammed, T. G. Asere and T. F. Diriba, *ACS Omega*, 2024, **9**, 2480–2490.
39 M. M. Khan, N. H. Saadah, M. E. Khan, M. H. Harunsani, A. L. Tan and M. H. Cho, *BioNanoScience*, 2019, **9**, 334–344.
40 A. S. Abdelbaky, T. A. Abd El-Mageed, A. O. Babalghith, S. Selim and A. M. H. A. Mohamed, *Antioxidants*, 2022, **11**, 1444.
41 P. Ramesh, K. Saravanan, P. Manogar, J. Johnson, E. Vinoth and M. Mayakannan, *Sens. Bio-Sens. Res.*, 2021, **31**, 100399.
42 X. Xiao, B. Peng, L. Cai, X. Zhang, S. Liu and Y. Wang, *Sci. Rep.*, 2018, **8**, 7571.
43 R. Kumar, S. Anandan, K. Hembram and T. Narasinga Rao, *ACS Appl. Mater. Interfaces*, 2014, **6**, 13138–13148.
44 K. Ravichandran, S. Snega, N. Jabena Begum, K. Swaminathan, B. Sakthivel, L. Rene Christena, G. Chandramohan and S. Ochiai, *Superlattices Microstruct.*, 2014, **69**, 17–28.
45 S. Vasantharaj, S. Sathiyavimal, P. Senthilkumar, V. N. Kalpana, G. Rajalakshmi, M. Alsehli, A. Elfasakhany and A. Pugazhendhi, *J. Environ. Chem. Eng.*, 2021, **9**, 105772.
46 N. M. Flores, U. Pal, R. Galeazzi and A. Sandoval, *RSC Adv.*, 2014, **4**, 41099–41110.
47 X. Chen, Z. Wu, D. Liu and Z. Gao, *Nanoscale Res. Lett.*, 2017, **12**, 143.
48 C. Jayakrishnan, S. R. Sheeja, J. Duraimurugan, S. Prabhu, R. Ramesh, G. S. Kumar, P. Maadeswaran and M. Shkir, *J. Mater. Sci. Mater. Electron.*, 2022, **33**, 9732–9742.

49 M. Ravbar, A. Kunčič, L. Matoh, S. Smole Možina, M. Šala and A. Šuligoj, *RSC Adv.*, 2022, **12**, 31235–31245.
50 A. Zyoud, A. H. Zyoud, S. H. Zyoud, H. Nassar, S. H. Zyoud, N. Qamhieh, A. Hajamohideen and H. S. Hilal, *Environ. Sci. Pollut. Res.*, 2023, **30**, 68435–68449.
51 S. Azizi, R. Mohamad, A. Bahadoran, S. Bayat, R. A. Rahim, A. Ariff and W. Z. Saad, *J. Photochem. Photobiol., B*, 2016, **161**, 441–449.
52 M. Schmitt and F. Heib, *RSC Adv.*, 2014, **4**, 17639.
53 N. T. Nguyen and V. A. Nguyen, *J. Nanomater.*, 2020, **2020**, 1–8.
54 M. O. Chijioke-Okere, N. J. Okorocha, B. N. Anukam and E. E. Oguzie, *Int. Lett. Chem., Phys. Astron.*, 2019, **81**, 18–26.
55 A. Balcha, O. P. Yadav and T. Dey, *Environ. Sci. Pollut. Res.*, 2016, **23**, 25485–25493.